Diagnosing the Intercept Parameters of the Exponential Drop Size Distributions in a Single-Moment Microphysics Scheme and Impact on Supercell Storm Simulations

CHARLOTTE E. WAINWRIGHT

School of Meteorology, and Center for Analysis and Prediction of Storms, and Advanced Radar Research Center, University of Oklahoma, Norman, Oklahoma

DANIEL T. DAWSON II

Center for Analysis and Prediction of Storms, University of Oklahoma, Norman, Oklahoma

MING XUE

School of Meteorology, and Center for Analysis and Prediction of Storms, University of Oklahoma, Norman, Oklahoma

GUIFU ZHANG

School of Meteorology, and Advanced Radar Research Center, University of Oklahoma, Norman, Oklahoma

(Manuscript received 2 August 2013, in final form 15 May 2014)

ABSTRACT

In this study, power-law relations are developed between the intercept parameter N_0 of the exponential particle size distribution and the water content for the rain, hail, graupel, and snow hydrometeor categories within the Milbrandt and Yau microphysics scheme. Simulations of the 3 May 1999 Oklahoma tornadic supercell are performed using the diagnostic relations for rain only and alternately for all four precipitating species, and results are compared with those from the original fixed-N_0 single- and double-moment versions of the scheme. Diagnosing N_0 for rain is found to improve the results of the simulation in terms of reproducing the key features of the double-moment simulation while still retaining the computational efficiency of a single-moment scheme. Results more consistent with the double-moment scheme are seen in the general storm structure, the cold-pool structure and intensity, and the number concentration fields. Diagnosing the intercept parameters for all four species, including those for the ice species, within the single-moment scheme yields even closer agreement with the double-moment simulation results. The decreased cold-pool intensity is very similar to that produced by the double-moment simulation, as is the areal extent of the simulated storm. The diagnostic relations are also tested on a simulated squall line, with similar promising results. This study suggests that, when compared with traditional fixed intercept parameters used in typical single-moment microphysics schemes, results closer to a double-moment scheme can be obtained through the use of diagnostic relations for the parameters of the particle size distribution, with little extra computational cost.

1. Introduction

As numerical weather prediction models gain convection-resolving grid spacings of 1 km or less, the parameterization of microphysical processes becomes critical. In general, bulk microphysics (MP) parameterizations, which specify a particular size distribution (PSD) for each hydrometeor species and predict certain moments of the size distribution (e.g., the water mass, proportional to the third moment of the size distribution), are used because of the comparatively high cost of nonbulk spectral or bin models for simulations of three-dimensional moist convection.

The most commonly used PSD for precipitating hydrometeors is the inverse exponential distribution, which can be written as

Corresponding author address: Ming Xue, Center for Analysis and Prediction of Storms, University of Oklahoma, 120 David L. Boren Blvd., Suite 2500, Norman, OK 73072.
E-mail: mxue@ou.edu

DOI: 10.1175/JAMC-D-13-0251.1

$$N(D) = N_0 \exp(-\Lambda D), \quad (1)$$

where N_0 is the intercept parameter, Λ is the slope parameter of the PSD, and D is drop diameter. Parameter N_0 is usually assigned a fixed value for each category in single-moment (SM) MP schemes. The most well known of these exponential distributions is the Marshall–Palmer (Marshall and Palmer 1948) distribution, which specifies the rain intercept parameter N_{0r} to be $8 \times 10^6\,\mathrm{m}^{-4}$. Use of this fixed value for N_{0r} has been shown to be restrictive, however, because N_{0r} can vary significantly within single precipitation events both spatially and temporally (Tokay and Short 1996; Zhang et al. 2008; Waldvogel 1974). Snook and Xue (2008) investigated the effect of varying N_0 for the rain and hail PSDs on storm evolution within high-resolution supercell simulations, focusing on the effect upon tornadogenesis. It was found that, in simulations in which N_0 was lowered such that the PSD favored large drops or hailstones, the resulting cold pools were weaker and the simulations tended to develop into single or multiple supercells, whereas when N_0 was increased the storms transformed to a linear mode during the simulations. Tornado-like low-level vortices formed in the low-N_0 simulations but not in others. Cohen and McCaul (2006) performed simulations using an increased median volume diameter for hail and graupel, equivalent to decreasing the N_0 value for those species, which resulted in reduced low-level cooling because of decreased melting. Earlier studies of van den Heever and Cotton (2004) and Gilmore et al. (2004) also found significant sensitivity of simulated supercell storms to PSD parameters. Morrison et al. (2009), Dawson et al. (2010, hereinafter DXMY10), and Yussouf et al. (2013) more recently compared SM and double-moment (DM) MP schemes for simulations of squall lines and supercells, respectively (DXMY10 also considered a triple-moment scheme), likewise finding large sensitivity to the number of moments predicted, with the DM schemes typically performing better than their SM counterparts. Van Weverberg et al. (2011) investigated the impact of PSD assumptions in an SM MP scheme on precipitation and storm dynamics, and the sensitivity of a simulated squall line to two-moment MP complexity (Van Weverberg et al. 2012).

The distribution represented by (1) is a special case of the gamma distribution (Ulbrich 1983), which has the form

$$N(D) = N_0 D^{\alpha} \exp(-\Lambda D), \quad (2)$$

where α is the shape parameter, a dimensionless measure of the spectral width of the distribution. If α is set to 0, the distribution is reduced to the inverse exponential form. The addition of the shape parameter allows the gamma distribution to depict a far greater range of PSDs than the inverse exponential distribution. Mallet and Barthes (2009) applied a maximum likelihood technique to categorize raindrop size distributions (DSDs) from optical disdrometer data and found that 91% of the measured DSDs were of the gamma type.

The values of the gamma distribution parameters vary widely in nature, both between and within a given precipitation event; thus, parameterizing any of them as constant will introduce a source of error into the MP. Ulbrich (1983) calculated a typical range of values for α and N_0 of the rain DSD, encompassing relations derived from reflectivity–rain-rate (Z–R) relationships presented in a number of other studies. Calculated values for α varied from -3.42 to 5.04 (the range was far narrower for studies that were based on convective rain, with α ranging from 0.40 to 1.63), and values for N_0 ranged from 1.29×10^3 to $9.20 \times 10^{12}\,\mathrm{m}^{-4}$ (from 7.05×10^6 to $2.46 \times 10^8\,\mathrm{m}^{-4}$ for convective rain). Although some of the variations in parameter values are due to errors in measurements, modeling, and fitting procedures (Cao and Zhang 2009), variation due to physical causes appears to dominate (Zhang et al. 2003; Milbrandt and Yau 2005a,b, hereinafter MY05a and MY05b, respectively).

The role of the shape parameter α was investigated in detail by MY05a, who showed that the rate of gravitational particle size sorting was dependent on α, with the size-sorting rate decreasing as α increases and approaching 1 as α becomes large. Size sorting is an intrinsic process within supercell evolution, as witnessed by the occurrence of the differential reflectivity Z_{DR} arc within supercells (Kumjian and Ryzhkov 2008). Hence it is important to parameterize the PSD in a realistic manner, allowing all parameters to vary as appropriate.

Thus, one way to improve an MP scheme is to increase the number of predicted moments of the PSD (Straka and Mansell 2005; MY05a). How the moments of the PSD are calculated depends on the way the PSD is parameterized. For the gamma distribution, the nth moment is calculated as

$$M_n = N_0 \Lambda^{-(\alpha+n+1)} \Gamma(\alpha + n + 1). \quad (3)$$

Most bulk MP schemes only predict one moment of the distribution, typically the third moment M_3, which is proportional to the hydrometeor mixing ratio q. In this case, it is usually the slope parameter Λ that is effectively prognostic while N_0 and α are held constant. In recent years, MP schemes that predict two or more moments have become increasingly popular, particularly for convective-scale modeling. Most of the DM schemes available predict both q and N_0, leaving α held constant while N_0 and Λ are directly linked to the predicted variables (e.g., MY05b; Morrison et al. 2005).

Data assimilation methods have been more recently employed for PSD parameter estimation and to test the sensitivity of model outputs such as precipitation to the value of certain PSD parameters. Tong and Xue (2008a,b) used an ensemble Kalman filter for simultaneous estimation of the model state and MP parameters, including N_0 for rain, snow, and hail. Model-output-state sensitivity to PSD parameter values has been investigated using a Markov chain Monte Carlo algorithm to produce joint probability density functions of the model output state and PSD parameters (Posselt and Vukicevic 2010). The joint PDFs for model output state and N_0 for snow and graupel (N_{0s} and N_{0g}) were shown to exhibit multimodality as a result of a transition from convective precipitation to stratiform precipitation (Posselt and Bishop 2012). The transition from convective precipitation to stratiform precipitation has also been shown to alter the joint PDFs for MP processes such as evaporation and N_0 of rain, snow, and graupel (van Lier-Walqui et al. 2012). This fact further illustrates that using a single fixed value for N_0 for all types of simulation is not appropriate. As an alternative way of addressing microphysics uncertainties, van Lier-Walqui et al. (2014) proposed to estimate uncertain factors multiplying various microphysical-process rate terms in MP parameterization schemes, using an ensemble Kalman filter.

Aside from moving to multimoment schemes, which are computationally expensive, other methods of extending low-moment schemes beyond the fixed single-parameter approach have been attempted. The most common method relates a free parameter in the PSD to another independently predicted PSD parameter. Zhang et al. (2001) investigated relations between the PSD parameters using video disdrometer data collected in Florida and derived a relation between the shape and slope parameters. The α–Λ relation was subsequently updated using disdrometer measurements for rain DSDs observed in Oklahoma (Cao et al. 2008).

Zhang et al. (2008) used the same disdrometer data as Cao and Zhang (2009), gathered in central Oklahoma during the summers of 2005–07, to derive a relationship between N_0 of the inverse exponential PSD and the rainwater content W_r (which, like mixing ratio q_r, is proportional to the third moment of the distribution). The diagnostic relation was formed using the method of moment relations, outlined in detail in their paper. Their derived relation for rain was $N_{0r}(M_2, M_4) = 7106W_r^{0.648}$, where N_{0r} is measured in number per meter cubed per millimeter and W_r is in grams per meter cubed. Here, N_{0r} is given as a function of M_2 and M_4 because its relation is derived from these two moments.

In the SM version of the Milbrandt and Yau (MY) MP scheme (MY05b), described in more detail in section 3, the PSD of each precipitating hydrometeor category is modeled by a gamma distribution with a fixed value of α. In this paper, we assume α to be zero, leading to the exponential distribution commonly used in SM and DM schemes.

Given the moment relation in (3) and setting α to zero, we see that the exponential PSD parameters, N_0 and Λ, can be determined using any two moments of the distribution. Given any two moments M_j and M_k, the PSD parameters can be calculated as

$$N_0 = \frac{M_j \Lambda^{j+1}}{\Gamma(j+1)} \quad \text{and} \tag{4}$$

$$\Lambda = \left[\frac{M_j \Gamma(k+1)}{M_K \Gamma(j+1)}\right]^{1/(k-j)} . \tag{5}$$

The moment estimates from disdrometer measurements contain errors (Zhang et al. 2008), causing errors in the DSD parameters determined from them. The middle (second and fourth) moments were used in their study because they contain the least error (Cao and Zhang 2009). The main issue with these observation-based studies is that the diagnostic relations are derived using disdrometer data collected at the surface, primarily for rain. Aircraft observational campaigns have also provided information on the DSDs of rain (e.g., Beard et al. 1986; Yuter and Houze 1997), snow (e.g., Houze et al. 1979; Field et al. 2005), and ice (e.g., Heymsfield et al. 2006). Diagnostic relations derived from three-dimensional datasets for individual species are needed for use within MP parameterization schemes.

The goal of this study is to formulate and test diagnostic relationships between N_0 and W for each precipitating hydrometeor species and to implement these relationships within the SM MY MP scheme (MY05b) available within the Advanced Regional Prediction System (ARPS) model (Xue et al. 2000, 2001). It is hypothesized that this approach should allow a more realistic PSD model than the use of a fixed value of N_0 for each precipitating hydrometeor species and will enable a more accurate representation of the PSDs. To this end, the overall aim of the study is to bring the results of the SM MP scheme more in line with the results of the corresponding DM MP scheme. For the derivation of the PSD parameter relationships in this study, the zeroth and third moments of the inverse exponential PSD are used since these are independently predicted within the DM MY MP scheme. As the first proof-of-concept attempt and because of the general lack of DSD observations for multiple species in 3D volumes, we use the output of the

MY DM simulation to derive the relations. We leave to future work an investigation of the representativeness of surface DSDs relative to those aloft for the purpose of formulating diagnostic relations.

The remainder of the paper is organized as follows: the case being simulated is described in section 2. The formulation of the diagnostic-N_0 relationships is covered in section 3. The setup used for the numerical experiments is described in section 4. Section 5 includes results of the experiments and discussion. Section 6 summarizes the results and discusses future work.

2. The 3 May 1999 Oklahoma tornadic supercell case

On 3 May 1999, one of the most significant tornado outbreaks ever to occur in the United States caused extensive damage across Oklahoma and Kansas, including the metropolitan areas of Oklahoma City and Wichita. Fifty-eight tornadoes struck within the county warning area of the Norman, Oklahoma, National Weather Service Weather Forecast Office over a period of 8 h (Speheger et al. 2002). Sixteen of these tornadoes were rated F2 or greater on the Fujita (1971) scale, including two F4 tornadoes and one F5 tornado. The F5 tornado tracked through the small community of Bridge Creek, parts of Moore, southern Oklahoma City, Del City, and Midwest City, causing 36 direct fatalities (Brooks and Doswell 2002) and injuring 583 people.

Observations from the Oklahoma Mesonet (Brock et al. 1995) and mobile mesonets (Markowski 2002) indicated that the cold pools associated with the tornadic supercells in central Oklahoma were mainly small and relatively weak. The synoptic setup for the event exhibited a large-scale trough located over the western Unites States, with an embedded short-wave trough over Arizona. The large-scale trough amplified as it passed over the Rocky Mountains, and the short-wave trough propagated over western Oklahoma and Kansas, while a deepening surface low was located over the central high plains (Thompson and Edwards 2000). The low-level flow was south-to-southeast over the southern Great Plains. More detail on the synoptic setup for the event can be found in Thompson and Edwards (2000) and Roebber et al. (2002).

Given the inherent instability present, a gap in the cirrus cloud cover allowed a cumulus tower to develop close to Lawton in southwestern Oklahoma, around 2030–2045 UTC. This evolved into the first supercell and, after an initial split, rapidly developed into a right-moving supercell—storm A (Thompson and Edwards 2000). Storm A became tornadic and produced at least 14 distinct documented tornadoes between 2151 UTC 3 May and 0125 UTC 4 May (Speheger et al. 2002). The most intense of the tornadoes produced by storm A was A9, the F5 tornado that left a 37-mile trail of destruction through the communities of Bridge Creek, Moore, and Oklahoma City. DXMY10 simulated a supercell storm within an environment believed to be representative of the environment in which storm A developed, and the study found substantial sensitivity of the simulated supercell storm to the number of moments predicted with versions of the MY scheme. Their predicted cold pool was generally too strong when using a single-moment scheme, while that predicted using a three-moment scheme was found to be the best.

3. Diagnostic relations for N_0

As pointed out previously, DSD observations for multiple species in 3D volumes are generally unavailable, making it difficult to obtain diagnostic relations for several species that are applicable to the entire storm. As the first proof-of-concept attempt, we use the output of a DM simulation for the 3 May 1999 case to derive diagnostic relations for use in an SM scheme. This allows us to see how close the results of an SM scheme with diagnostic relations can be to those of a DM scheme.

Using a single sounding to define the storm environment, DXMY10 have shown that, for the 3 May 1999 case, the simulated supercell is sensitive to the use of single-, double-, and triple-moment options of the MY scheme. A similar sensitivity to the moment of the MY scheme used was shown for another supercell simulation in Milbrandt and Yau (2006). DXMY10 showed that the DM (and triple moment) MP simulation produced a surface cold pool of strength closer to that observed by the Oklahoma Mesonet (their Figs. 1 and 6) and that the reflectivity from the DM simulation compared more favorably to observations than that of their SM simulation (DXMY10, their Figs. 6 and 7).

In this study, the output of a horizontally homogeneous idealized simulation with 500-m grid spacing and using the DM version of the MY scheme with α set to zero and using the same sounding as in DXMY10 is used as a "synthetic dataset" to derive the diagnostic relations for N_0 for each category. This simulation will hereinafter be referred to as the MY2 or "reference" simulation. The derived diagnostic relations are then implemented in the SM option of the MY scheme for the various experiments in this study.

Model output of the zeroth and third moments for each precipitating hydrometeor category (rain, snow, graupel, and hail) was taken every 300 s throughout the second hour of MY2 and collated into a single large dataset. Data at grid points in the full domain were included

TABLE 1. The fixed N_{0x} values used in the original MY single-moment microphysics scheme, the derived diagnostic relation for N_{0x}, and the mean N_{0x} values from simulation MY2 for rain, snow, graupel, and hail.

Species	Default fixed N_{0x} values	Diagnostic relation derived from MY2 simulation	Mean N_{0x} from MY2 simulation
Rain	$N_{0r} = 8 \times 10^6\,\mathrm{m}^{-4}$	$N_{0r} = 1.16 \times 10^5 W_r^{0.477}\,\mathrm{m}^{-4}$	$N_{0rm} = 1.18 \times 10^5\,\mathrm{m}^{-4}$
Snow	$N_{0s} = 3 \times 10^6\,\mathrm{m}^{-4}$	$N_{0s} = 4.58 \times 10^9 W_s^{0.788}\,\mathrm{m}^{-4}$	$N_{0sm} = 3.95 \times 10^8\,\mathrm{m}^{-4}$
Graupel	$N_{0g} = 4 \times 10^5\,\mathrm{m}^{-4}$	$N_{0g} = 9.74 \times 10^8 W_g^{0.816}\,\mathrm{m}^{-4}$	$N_{0gm} = 5.26 \times 10^7\,\mathrm{m}^{-4}$
Hail	$N_{0h} = 4 \times 10^4\,\mathrm{m}^{-4}$	$N_{0h} = 5.25 \times 10^5 W_h^{0.411}\,\mathrm{m}^{-4}$	$N_{0hm} = 3.50 \times 10^5\,\mathrm{m}^{-4}$

in the file, although, because vertical grid stretching was employed, the low levels are more heavily sampled than the upper levels. Points were included provided that a minimum threshold of hydrometeor mixing ratio was met. This threshold was purposely kept low at $1 \times 10^{-5}\,\mathrm{kg\,kg^{-1}}$ for each hydrometeor category to accurately represent the full range of mixing ratios produced by the simulation in the main precipitating region of the storm while still cutting small, noisy values outside the storm. For each point, the parameters of the inverse exponential distribution were calculated and the mass content W was derived using

$$W = 1000\rho_a q, \qquad (6)$$

where W is in grams per meter cubed, air density ρ_a is in kilograms per meter cubed, and mixing ratio q is in kilograms per kilogram. As in Zhang et al. (2008), we wish to form a power-law relation between W and N_0 of the exponential distribution for each species. In our case, these relations are calculated by performing a least squares minimization on both variables to give an effective linear relation between the logarithms of the variable pair. Transforming the variables back from logarithmic into linear space provides a power law for N_0 in terms of W. The coefficient and power of the derived N_0–W relationships were averaged across the examined model output times to give a more general relation for each precipitating hydrometeor category. In addition, the mean N_0 for each hydrometeor category was computed (Table 1). The plot showing the resulting dependence of N_0 on W (along with the time-averaged power-law fit) from the full dataset exhibits a high degree of scatter for rain (Fig. 1) and hail (Fig. 4, described below), and indeed, in the case of rain, the power-law fits for individual times varied substantially (Fig. 1, thin dashed lines). Average values of correlation coefficient squared for rain and hail are accordingly low (0.08 and 0.11, respectively). The averaged fit for rain (thick dashed line in Fig. 1) represented well the overall trend in the aggregated data, however. For all other categories, the power-law fits for individual times did not vary significantly across the range of times examined (thin dashed lines in Figs. 2–4), which suggests confidence in the robustness of the time-averaged derived relations. Last, the two-sided p values, using a hypothesis test in which the null hypothesis is that the slope is zero, were very close to zero for all fits, likely because of the large number of points used.

The MY suite of MP schemes contains four frozen hydrometeor categories—ice, snow, graupel, and hail, and each of these is handled separately within the ice phase processes. The ice total number concentration N_{ti} is already diagnosed on the basis of temperature in the SM option according to Cooper (1986). For rain and the other three frozen categories, the number concentration is calculated as the zeroth moment of the distribution using N_0 of the PSD of that species, which is set to a constant value for each species in the original SM MP scheme (see Table 1). Scatterplots showing the dependence of N_0 on W for snow, graupel, and hail are shown in Figs. 2–4. The fixed N_0 values and the diagnostic power-law relations

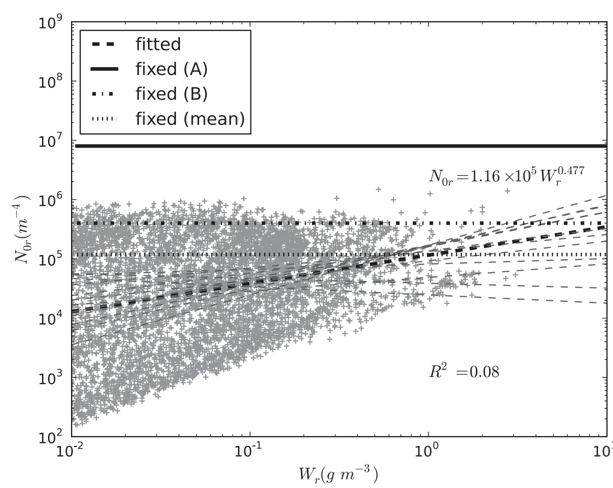

FIG. 1. Scatterplot and fits of rain intercept parameter N_{0r} vs water content W_r from MY2. For clarity, only every 100th point used in the fits is plotted. The N_{0r}–W_r pairs are directly computed from the predicted zeroth and third moments of the exponential DSD. The thick dashed line shows the average derived fitted relation (in linear space), thin dashed lines show the derived fits for individual times (every 300 s in the second hour of the simulation), the solid line shows the original fixed value of N_{0r} used in the MY1A experiment, the dash–dotted line shows the reduced N_{0r} used in experiment MY1B, and the dotted line shows the mean N_{0r} (from MY2) used in experiment MY1M.

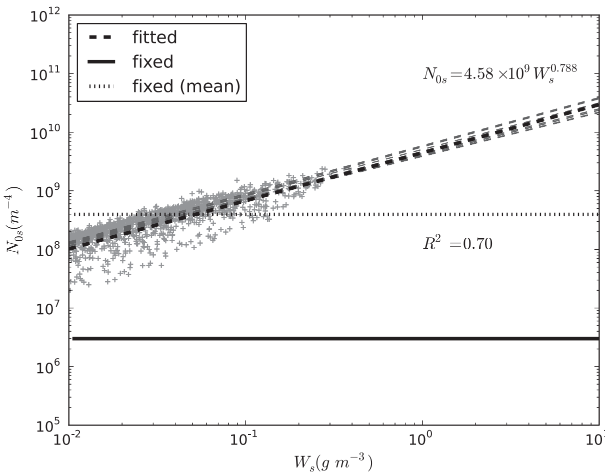

FIG. 2. As in Fig. 1, but for snow.

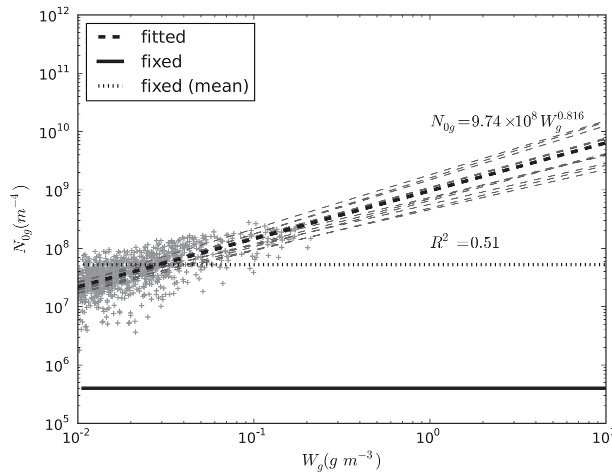

FIG. 3. As in Fig. 1, but for graupel.

used in the various SM MY experiments to be discussed in the next section are also shown in Figs. 1–4. In examining Figs. 1–4 and Table 1, it is clear that for each of the hydrometeor species the coefficient differs significantly from the default fixed value of N_0, by up to three orders of magnitude in the cases of snow and graupel.

The time dependence of the coefficient and power in the N_0–W relationships was examined (Fig. 5), and no significant time trends were found for any of the four species. It is clear that the rain category demonstrates much variability in the power of the N_{0r}–W_r relation, but this variability does not appear to be a function of time.

4. Numerical experiments

To test the diagnostic-N_0 relations, several simulations of the 3 May 1999 case were performed. The main aim of this study is to implement the diagnostic relations for N_0 within an SM MP scheme and to determine how well such an SM scheme reproduces the results of DM scheme. We perform several experiments, using the naming convention MY#X, where # is the number of moments prognosed, either 1 or 2, and X is a one- or two-letter variation identifier, described below and in Table 2. First, the reference DM simulation, MY2, is produced, and the diagnostic-N_0–W relations and average N_0 values are computed from its output, as described previously. A baseline SM simulation is then produced, using the original MY1 scheme (with the default constant N_0 for each category), denoted MY1A. The results of the following diagnostic-N_0 simulations are compared with these to gauge the impact and effectiveness of the diagnostic relations. Two more fixed-N_0 simulations were performed: 1) MY1B, using the MY1 scheme with N_{0r} lowered from 8×10^6 to $4 \times 10^5\ \mathrm{m}^{-4}$, and 2) MY1M ("M" for "mean"), using the average N_0 for each category derived from the MY2 reference simulation. The reduced value of $4 \times 10^5\ \mathrm{m}^{-4}$ for N_{0r} in MY1B is smaller by a factor of 20 than the default Marshall–Palmer (Marshall and Palmer 1948) DSD value but is still within the known uncertainty range of N_{0r} (Tong and Xue 2008a) and was also examined in DXMY10 for its impact on the simulation of a supercell storm. The reduced value corresponds to a DSD having more larger drops, a situation that typically leads to less evaporation and a weaker cold pool (DXMY10; Snook and Xue 2008).

Last, two further simulations were performed using the derived diagnostic-N_0 relations, one in which only the rain category used the diagnostic relation, and one in which N_0 for all categories, including four precipitating hydrometeors in total, is diagnosed. These are denoted MY1DR and MY1DA (for "diagnostic rain" and "diagnostic all"), respectively. For each of the SM simulations, the cloud

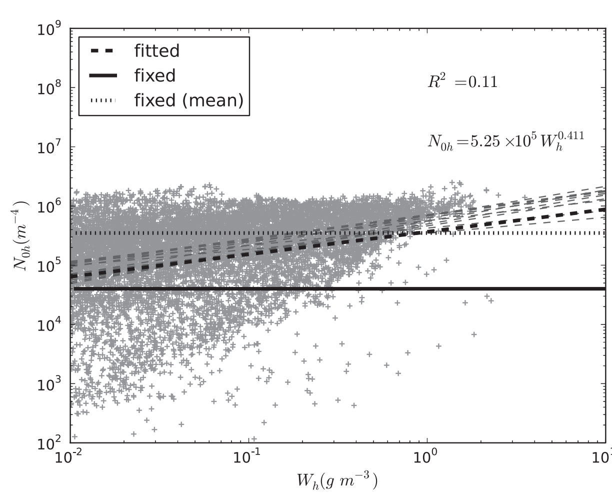

FIG. 4. As in Fig. 1, but for hail.

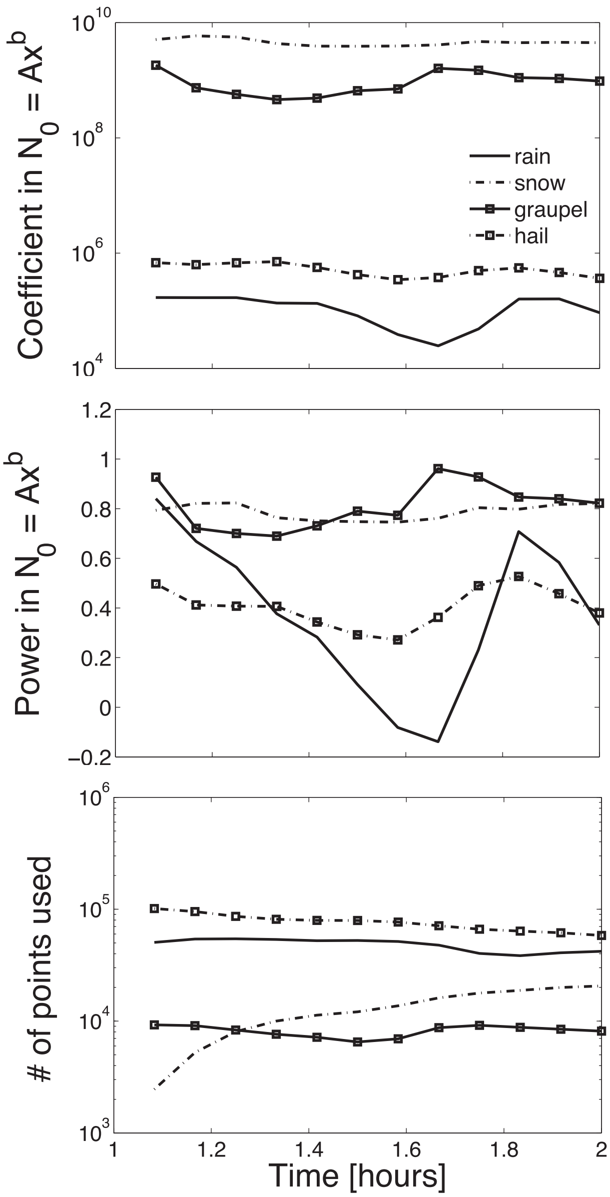

FIG. 5. Variation with time of the (top) coefficient A and (middle) power b in the $N_0 = Ax^b$ relation for each of the four hydrometeor species considered. (bottom) The number of points used to determine the relations for each species.

water fixed total number concentration N_{tc} remains at the default value, and again the cloud ice total number concentration N_{ti} is diagnosed based on temperature, as is the default (both N_{tc} and N_{ti} are predicted in MY2). Details of the simulations and the nomenclature used can be found in Table 2. The diagnostic functions themselves were applied within the MP scheme (after update by the model dynamics) at the same locations in the code at which the original fixed N_0 values were used for computations. In the specific case of the ice species, this occurs 1) at the beginning of the MP scheme and 2) just before the call to sedimentation. In the case of rain, the function is also applied just before the computation of warm-rain processes and again before computation of evaporation.

TABLE 2. Description of the microphysical setup used in the six simulations that were performed at 500-m horizontal resolution.

Expt name	Details of microphysics scheme
MY2	Original double-moment Milbrandt and Yau scheme
MY1A	Original single-moment Milbrandt and Yau scheme
MY1B	Single moment with reduced fixed value of $N_{0r} = 4 \times 10^5\,\mathrm{m}^{-4}$
MY1M	Single moment with intercept parameter set to mean values from MY2 for all precipitating hydrometeor categories
MY1DR	Single moment with intercept parameter diagnosed for rain only
MY1DA	Single moment with intercept parameter diagnosed for all precipitating hydrometeor categories

Each 2-h simulation was performed using the ARPS model with the same single sounding and thermal bubble initialization procedure as in the idealized experiments of DXMY10 and the same horizontal grid spacing of 500 m. In the current study, however, for efficiency a reduced domain size of 96 km × 96 km × 20 km was used, and the mean storm motion was subtracted from the original wind profile. Otherwise the setup of the experiments was identical to that of DXMY10. The use of this idealized model setup allows more control over the experiments and represents at least part of the natural variability among storms and their environment. It also facilitates direct comparison with the results of DXMY10. In particular, the simulations MY1A and MY2 correspond to MY1 and MY2 from DXMY10.

Fifty-three vertical levels were used with vertical grid stretching employed, giving a vertical grid spacing that is 20 m at the surface and increases to 800 m at the upper boundary. The fourth-order monotonic computational mixing scheme of Xue (2000) was utilized with a coefficient of $0.0015\,\mathrm{s}^{-1}$. The initial ellipsoidal thermal bubble that was used to trigger the storm had a maximum potential temperature perturbation of 4 K, horizontal radius of 10 km and vertical radius of 1.5 km, and it was centered 1.5 km above the surface, 35 km from the west edge, and 25 km from the south edge of the domain. The sounding used in the simulation was extracted from a 1-h forecast of an earlier 3-km real-data simulation of this case, at a location upstream of the low-level inflow of the storms. This was the same sounding used in DXMY10, and full details of the original real-data simulation can be found in Dawson et al. (2007).

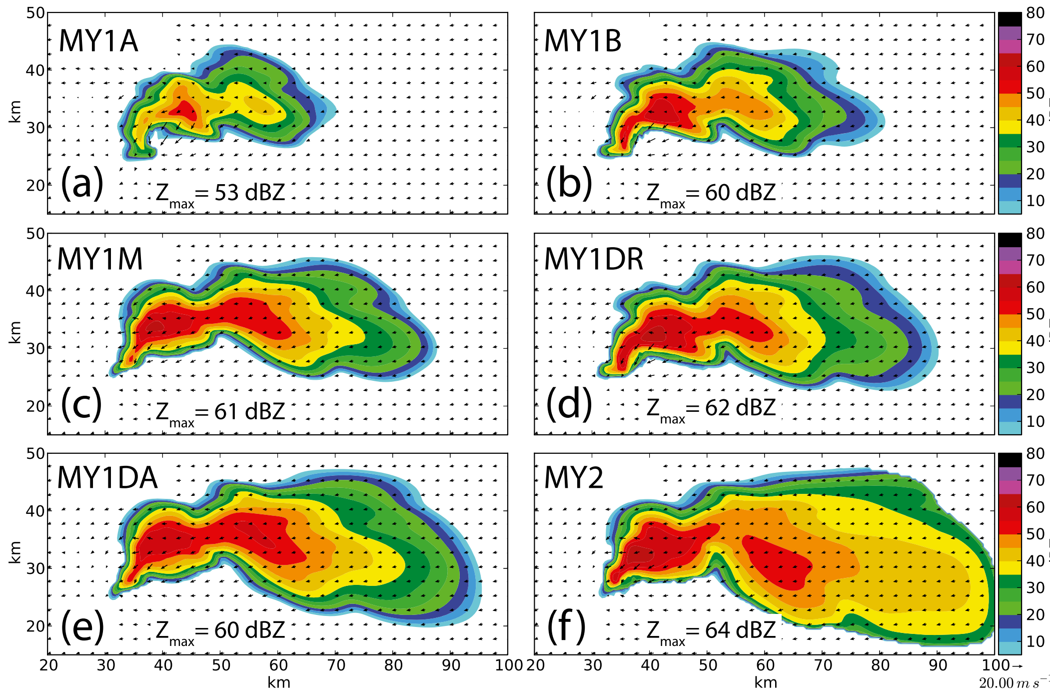

FIG. 6. Reflectivity (color fill) and horizontal wind vectors at the surface (plotted every 2.5 km) for a subset of the domain at 3600 s into the six simulations: (a) MY1A, (b) MY1B, (c) MY1M, (d) MY1DR, (e) MY1DA, and (f) MY2.

Each of the simulations in the current study was run for 2 h of simulation time. Van Weverberg (2013) noted that the short time scale of numerical simulations such as these does not sufficiently cover the entire convective cycle. For this reason, we note that the reported differences between the simulations in this study may not remain constant over the entire convective cycle.

5. Results and discussion

a. *Reflectivity structure*

The MY1A simulation produces a storm that by 1 h displays relatively low reflectivity values (Fig. 6a[1]; maximum of 53 dBZ) in its core and indeed begins to decay rapidly in the second hour (not shown), primarily as a result of a relatively strong, surging cold pool (Fig. 9a, described below). It also displays a forward flank region with a relatively small area when compared with each of the other experiments (Figs. 6b–f).

In contrast, the forward flank reflectivity region is much larger in MY2 (Fig. 6f) than in MY1A and is somewhat larger than that typically observed in supercell storms (e.g., Doswell and Burgess 1993). Morrison and Milbrandt (2011) found that the MY schemes produce long and narrow forward flank regions. Further tests (not shown) strongly suggest that this is due to the relatively low fall-speed curve of graupel used, but further investigation of this issue is beyond the scope of this paper. This does not affect the key point of this paper since we are primarily interested in how well the results of the SM scheme can match the DM, as a proof of concept. There are many processes that cannot be well represented within the SM scheme, however, such as size sorting. In contrast, the DM scheme does parameterize size sorting, although when the shape parameter α is set to 0 (as in MY2), excessive size sorting tends to occur (MY05a). We suggest that the sharp gradient at the leading edge of the forward flank reflectivity (Fig. 6f) is due to the effect of the excessive size sorting. Simulations of this case performed using the triple-moment MY scheme, which more accurately parameterizes size sorting (MY05a), produced a more gradual and realistic reflectivity gradient in this region (see Fig. 7 in DXMY10), corresponding more closely to radar observations of this case (DXMY10). In addition, a sensitivity test was performed in which the MY2 experiment was repeated with size sorting turned off (by setting the number-weighted fall speeds equal to the corresponding mass-weighted fall speeds), and this also resulted in a more gradual reflectivity gradient, similar to that of the SM experiments (not shown).

[1] In this and similar figures, only a subset of the full model domain is shown.

Both MY1B and MY1M, in which the rain N_0 is reduced from MY1A, are seen to produce a storm structure that is closer to that of MY2 than MY1A does, particularly on the leading edge or forward flank of the storm. The maximum reflectivity in MY1B is 60 dBZ, which is closer to that of MY2 (maximum of 64 dBZ) and is considerably increased from that of MY1A. Since the only difference between MY1B and MY1A is the reduction in the (fixed) value of N_{0r}, this would seem to indicate that the default value of $8 \times 10^6\,\mathrm{m}^{-4}$ for N_{0r} is too high for the type of severe convective case being simulated here; this is perhaps not surprising because the Marshall–Palmer relation was derived mainly for stratiform rain. For a given water content, increasing N_{0r} will decrease the median volume diameter, resulting in decreased reflectivity values. Despite the overall structure of the storm being closer to MY2 than to MY1A, the areal extent of the forward flank reflectivity region in MY1B is still much smaller in comparison with that in MY2. The areal extent of reflectivity values of greater than 30 dBZ at 3600 s is 207 km^2 in MY1A, 319 km^2 in MY1B, 467 km^2 in MY1M, and 1257 km^2 in MY2. For a threshold value of 50 dBZ, the corresponding areas covered are 10, 53, 123, and 172 km^2, respectively, illustrating the large forward flank region in MY2. The reason for the overall larger regions of higher reflectivity in MY2 is tied to the larger rain sizes predicted in this simulation relative to the others (not shown).

The surface reflectivity structure produced by MY1DR (Fig. 6d) is broadly similar to that of MY1B (Fig. 6b) and MY1M (Fig. 6c), although the lateral extent of the storm is slightly increased. The maximum reflectivity is similar to MY1B, MY1M, and MY2 (Figs. 6b,c,f). The forward flank region in MY1DR shows decreased strength of the east–west reflectivity gradient in the forward flank region (the reflectivity decreases to zero more gradually from west to east) than in the fixed-N_{0r} experiments (Fig. 6d), which corresponds more closely to base reflectivity observations from KTLX (0.5° tilt, not shown). The area with reflectivity of greater than 30 dBZ is 474 km^2, and that with reflectivity of greater than 50 dBZ is 127 km^2.

To investigate possibly closer similarity to the reference simulation MY2 in the forward flank region, the diagnostic relations for the N_0 of snow, hail, and graupel are implemented in MY1DA. In examining the reflectivity structure generated by MY1DA, (Fig. 6e) it is clear that the inclusion of diagnostic N_0 for graupel, snow, and hail has a large effect on the lateral extent of the storm and general storm structure. It was shown by Gilmore et al. (2004) that altering N_0 for hail and graupel caused large variations in the accumulated precipitation at the surface, and so it is reasonable to expect that altering the values of N_{0h} and N_{0g} should cause changes in several fields. The overall reflectivity structure is seen to resemble that of MY2 more closely than any other simulations. Particular increased similarity (relative to the MY2 simulation) is noticed in the forward flank region of the storm, with that of MY1DA being larger in size than in the other SM simulations. The areal extent of reflectivity of greater than 30 (50) dBZ at 3600 s is 686 (166) km^2, as compared with 1257 and 172 km^2 for MY2, respectively. This result would suggest that by diagnosing N_0 for the frozen categories we are able to represent more accurately the ice processes that contribute to fallout from the anvil. We discuss the impact on specific MP processes in section 5e.

Diagnosing N_{0r} produces a simulation closer to MY2 than do the fixed-N_{0r} SM simulations, but the increased similarity is mostly limited to the lowest levels, since the same fixed N_0 values for the ice categories are used in MY1DR as are used in MY1A, and little change is observed above the freezing level. This can be seen by an examination of the reflectivity structure above the melting level, at 5.5-km height (Fig. 7). MY1B and MY1DR show virtually no differences from MY1A (all have reflectivity magnitudes that are much too high as compared with MY2; cf. Figs. 7a,b,d with Fig. 7f), which is expected because only the rain PSD is altered in these simulations. To be more specific, the rain mixing ratios are comparable among MY1A, MY1B, and MY1DR, most of which is converted to hail in the updraft of the storm (not shown). Since, in the SM experiments, only mixing ratio is prognosed, once ice forms aloft its PSD is dictated solely by its own mixing ratio and N_0, the latter of which is the same fixed value for each ice category in MY1A, MY1B, and MY1DR. In contrast, MY1M and MY1DA both show reflectivity patterns and magnitudes that are much closer to that of MY2 (maximum reflectivities at 3600 s of 53, 52, and 47 dBZ, respectively; Figs. 7c,e,f), demonstrating the value of using either the mean or diagnosed N_0 for the ice categories.

Although the reflectivity structure at only a single time has been shown for the sake of brevity, the structure at other times is qualitatively consistent with the above analysis. Nevertheless it is instructive to examine the temporal evolution of the behavior in reflectivity. This is accomplished by computing the RMS difference at the surface for each of the SM simulations against that of MY2, for the duration of the 2-h simulations. The results are shown in Fig. 8. Consistent with the analysis of the plots at 3600 s above, MY1DA is closest to MY2 for the entire duration of the simulation period, showing the largest area of moderate reflectivity relative to MY2 (Fig. 8, top) and the lowest RMS difference of all of the SM experiments (Fig. 8, bottom). In contrast, MY1A clearly performs poorly across the entire simulation duration.

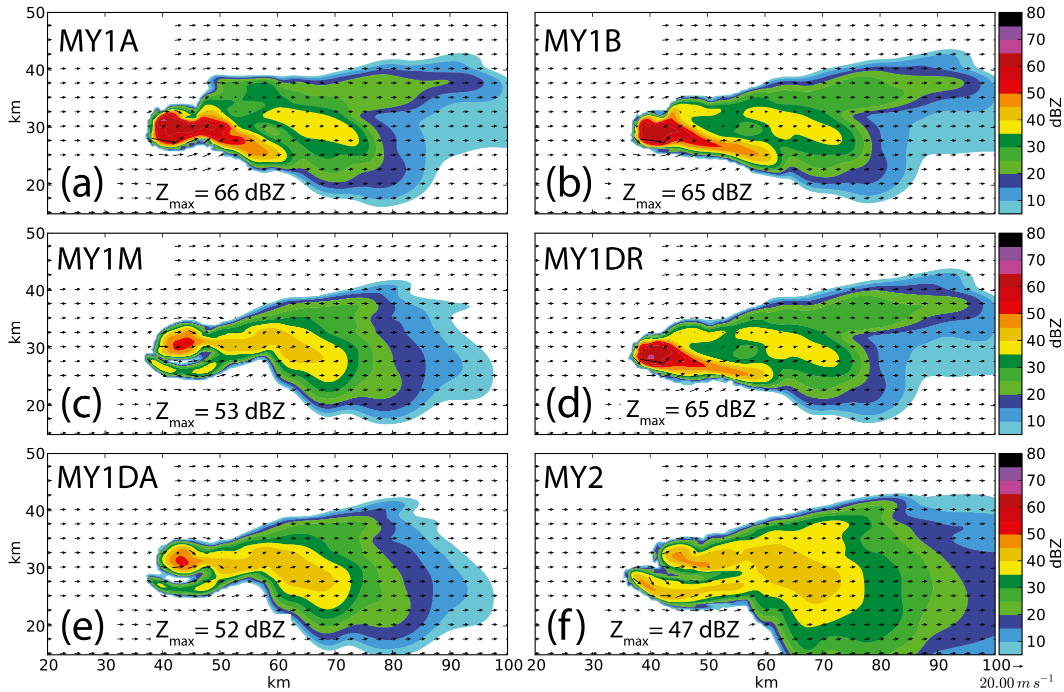

FIG. 7. As in Fig. 5, but for an altitude of ~5680 m.

b. Cold-pool structure

The cold pool is discussed in terms of the equivalent potential temperature perturbation θ_e' fields at the surface, as in DXMY10, since the θ_e' field also takes into account moisture effects. Here, θ_e is calculated according to Bolton (1980).

The cold pool produced in MY1A is seen to be strong (Fig. 9a), with a minimum θ_e' of -29 K at 3600 s. The areal extent of the cold pool as defined by a threshold of $\theta_e' < -1$ K also continues to increase with time during the simulation period (Fig. 10, top) In fact, it is the strength of the cold pool that cuts off the updraft after 1 h and causes the simulated storm to decay (not shown). In addition to having the largest θ_e' deficit, the areal extent of the cold pool at 3600 s is also the largest of any of the simulations, at 557 km^2. The time evolution of the cold pool in each experiment is quantified in Fig. 10, which shows total cold-pool area as defined above (Fig. 10, top), minimum θ_e' (Fig. 10, middle), and root-mean-square difference (RMSD) of surface θ_e relative to the reference experiment MY2. MY1A consistently shows the largest

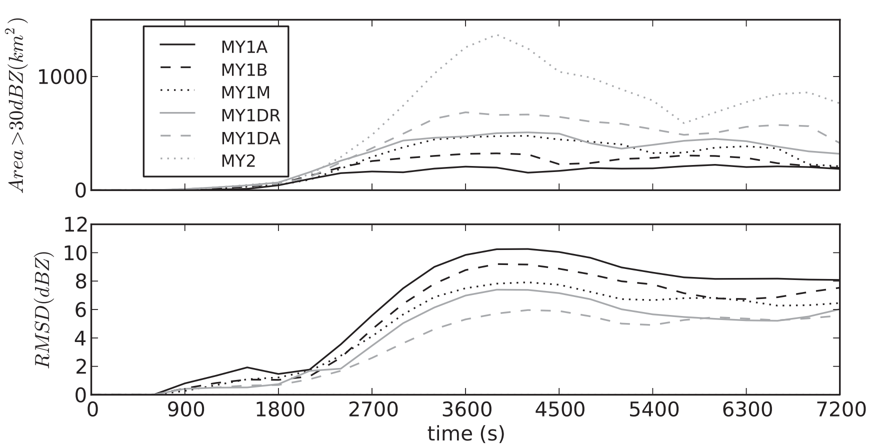

FIG. 8. (top) Area of surface reflectivity > 30 dBZ vs time for each of the experiments, and (bottom) RMS difference in surface reflectivity from experiment MY2 vs time for each of the single-moment experiments.

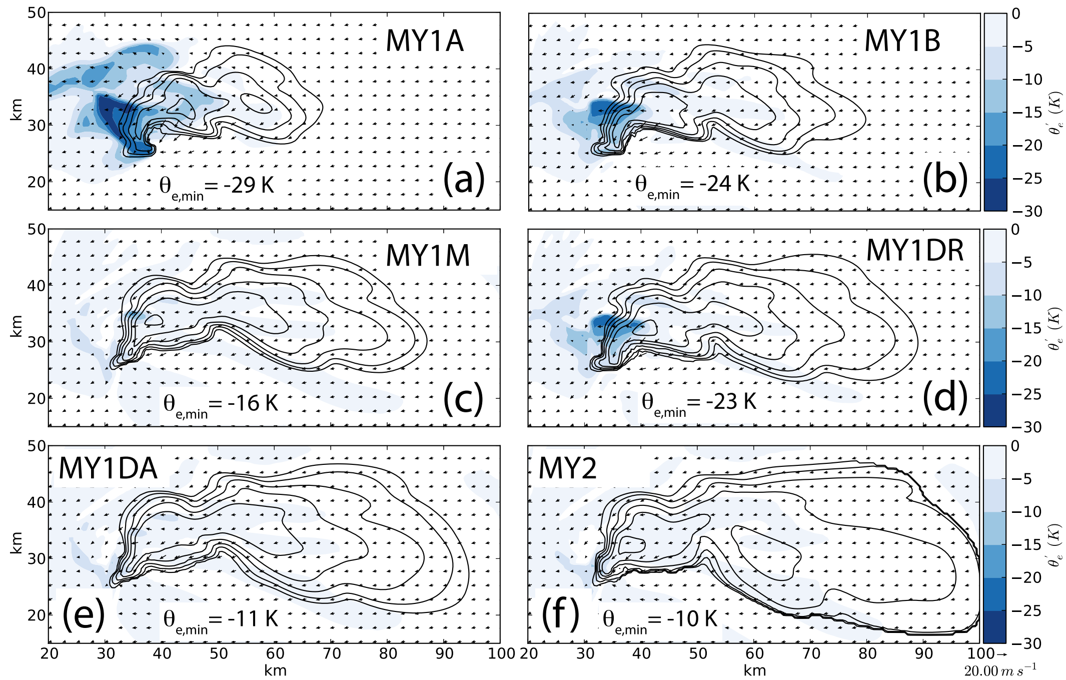

FIG. 9. As in Fig. 5, but for surface equivalent potential temperature perturbation (color filled) and reflectivity (contours, with 10-dBZ increment).

cold-pool area, smallest minimum θ_e', and highest RMSD of θ_e of any of the experiments.

The cold pool in MY2 is very weak in comparison, with a minimum θ_e' of -10 K, which is comparable to the minimum θ_e' observed by the mobile mesonet (Markowski 2002). The areal coverage of $\theta_e' < -1$ K at 3600 s is substantially less than in MY1A, at 205 km^2.

The cold pool produced by MY1B is weaker than that of MY1A, with a maximum θ_e deficit of -24 K, and an areal coverage of $\theta_e' < -1$ K of 358 km^2 at 3600 s. Several researchers (e.g., Milbrandt and Yau 2006; Snook and Xue 2008; DXMY10) found that simulations performed using reduced values for N_{0r} and N_{0h} tend to produce a relatively weak cold pool when compared with simulations performed using increased N_0 values. This behavior is due to distributions that favor fewer large particles possessing a reduced total hydrometeor surface area when compared with the same mass of water distributed as a large number of smaller particles. This reduced surface area limits the potential for evaporative and melting cooling, which are important mechanisms for cold-pool formation.

The cold-pool structure of MY1DR at 3600 s is similar to that of MY1B in terms of both maximum strength and areal coverage (cf. Fig. 9b with Fig. 9d), and its time evolution is also remarkably similar (Fig. 10 solid gray and black dashed lines, respectively). This indicates that simply reducing N_{0r} by a factor of 20 produces much the same benefit in this case as diagnosing N_{0r} in terms of the cold-pool structure and intensity. While a considerable decrease in cold-pool strength is seen from MY1A to MY1DR, the further decrease in cold-pool strength from MY1DR to MY1DA would suggest that the frozen categories have a comparable impact [as demonstrated for graupel in Van Weverberg et al. (2012)]. It is suggested that as the diagnostic relation changes the shape of the frozen categories PSD this modulation is reflected in changes in processes such as melting and collection of rain by hail. Using melting as an example, note, however, that in the case of the SM schemes the PSD of rain depends only on its unique N_0–W relation (whether fixed or diagnosed) and not on the PSD of the melting category, whereas the same is not generally true for a DM scheme.

Last, simulations MY1M and MY1DA, which involve using the fixed N_0 for each species using the mean value computed from MY2 and using the diagnostic relations derived from MY2, respectively, also show remarkably similar cold-pool structure and intensity at 3600 s (Figs. 9c,e). Both also compare very favorably to the MY2 cold pool at this time (Fig. 9f). The time evolutions of total cold-pool area and minimum θ_e' are also closer to MY2 than are any of the other SM simulations (Figs. 10, top and middle), while both have nearly identical RMS differences in θ_e against MY2 (Fig. 10, bottom).

From these results, either choosing more accurate fixed values of N_0 or the diagnostic approach clearly

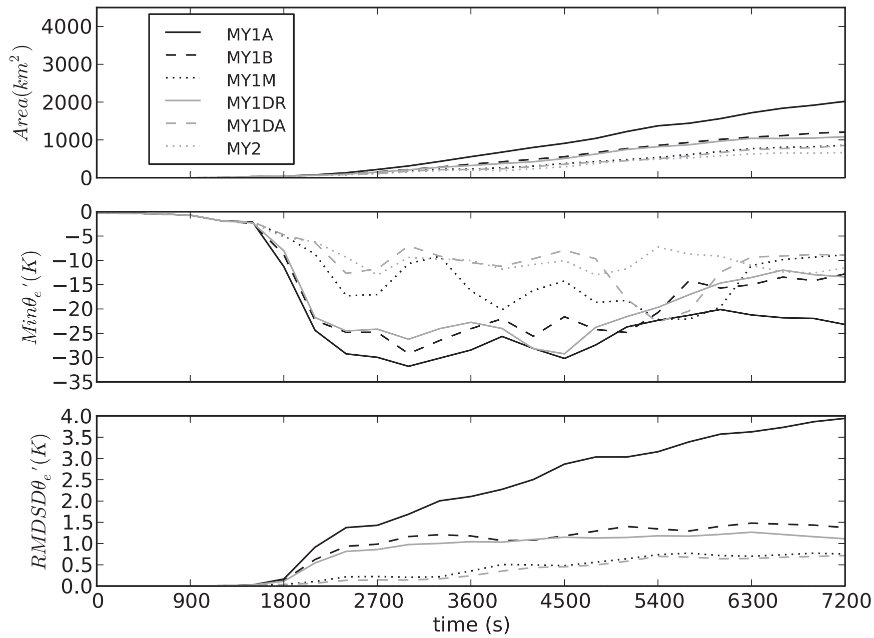

FIG. 10. Evolution of (top) total area of the cold pool as defined by all grid squares at the surface with $\theta_e' < -1$ K for each simulation, (middle) the minimum θ_e' in the cold pool for each simulation, and (bottom) the RMSD in θ_e for each of the five single-moment simulations when compared with MY2.

shows promise in producing cold pools that are closer to the DM results. Although reducing the strength of the cold pool is clearly not desirable in all cases, the goal of this study is to recreate the key features of the DM scheme, which in this case presented with a cold pool of significantly reduced strength from the default SM (MY1A) simulation.

c. *Total number concentration*

The striking differences in storm structure and cold pool among the experiments in this study exemplify the large impact that PSD parameters can have upon the simulation results. As demonstrated previously, altering N_0 affects the simulation indirectly through feedback from processes such as evaporative effects but also directly through the impact on N_t. An important test of the viability of the diagnostic-N_0 approach is to investigate how well the N_t fields are reproduced relative to the MY2 experiment, which explicitly predicts N_t (N_t in the single-moment schemes is diagnosed from q and N_0 for a given category). Following the approach above, we present plots of the rain total number concentration N_{tr} *at the surface* at 3600 s for each of the experiments in Fig. 11. Immediately it can be seen that there are large variations in both the magnitude and range of N_{tr} values across each of the single-moment simulations. In general, the diagnostic-N_{0r} simulations, MY1DR and MY1DA (Figs. 11d,e), compare most favorably in a qualitative sense to MY2 (Fig. 11f), particularly when considering the range of values from the core to the edge of the forward flank. In contrast, MY1A, MY1B, and MY1M (the fixed-N_0 simulations) all have a much different range of N_{tr} across the storm, although MY1B shows the closest maximum value of N_{tr} as compared with MY2 (462 and 342 m^{-3}, respectively). This behavior is reflected in the histograms of N_t shown in Fig. 12, which confirm that the diagnostic-N_0 simulations better capture the range and shape of the distribution of N_t in the simulations for each of the hydrometeor categories, whereas the fixed-N_0 simulations have histograms that, depending on the choice of the fixed value of N_0 in each case, exhibit only partial overlap with the range of values from MY2 (e.g., as in the case of N_{tr} for MY1A as compared with MY2; Fig. 12a). In general, none of the SM schemes fully captures the broad range of N_t values exhibited by the MY2 scheme for each category, but the diagnostic relations clearly outperform the fixed-N_0 simulations in this regard.

We note here that, even though similar results in terms of the cold-pool strength and precipitation structure seem obtainable by choosing a reasonable fixed value of the rain N_0 (such as in MY1B and MY1M), in practice it is difficult to predetermine what value should be used, and the constant fixed values are thus not necessarily realistic, as is shown above when considering the histograms of N_t. For this reason, we believe the

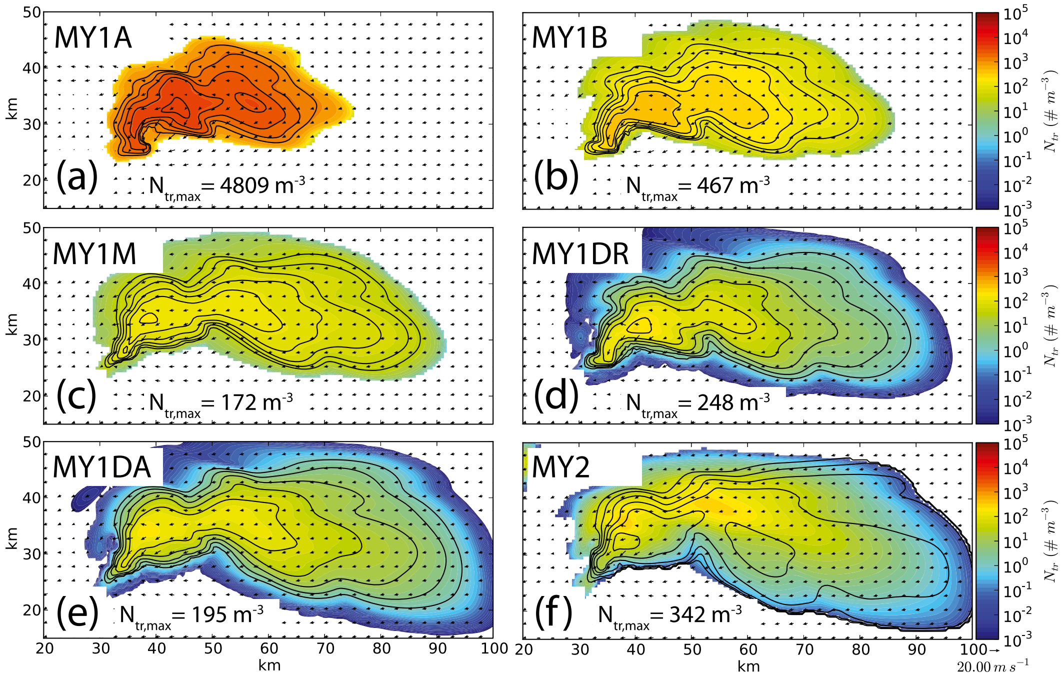

FIG. 11. As in Fig. 5, but for rain total number concentration N_{tr} (m^{-3}; color filled).

diagnostic relations hold more promise; to say the least, they provide spatial variability for the PSD parameters that should be more realistic than assigned constant values.

In terms of each of the variables examined in this study, consistent increase in similarity to MY2 is seen in MY1DR over MY1M, MY1B, and MY1A, in that order. Further similarity to MY2 in examined variables is seen in MY1DA, consistent with the goal of this study. This result is encouraging, and it is suggested that the method of diagnosing N_0 on the basis of independently predicted variables merits further investigation. We suggest that the diagnostic relationships be derived for additional cases besides supercells to investigate the representativeness of the relations derived in this study. An investigation into the dependence of the diagnostic relations on variables other than water content, such as temperature and updraft velocity, would also add value to this method. Although a diagnostic relation for N_0 brought the simulation results closer to the DM results, we recognize that there is a limit to this approach; there are intrinsic limits to the SM scheme. One example of these limits can be seen by examining carefully the pattern of N_{tr} in MY2 (Fig. 11f), which exhibits a dipole structure approximately straddling the centerline of the forward flank reflectivity region, with higher values to the north of this line and progressively smaller values to the south. This gradient in N_{tr} is associated with larger mean diameters of rain near the south edge of the forward flank and progressively smaller mean diameters toward the north (not shown), which is consistent with observed and simulated Z_{DR} arcs (e.g., Kumjian and Ryzhkov 2008, 2009, 2012; Jung et al. 2010; Snyder et al. 2010). This pattern is a reflection of raindrop size sorting, which again comes about in MY2 as a result of the differential sedimentation of the q and N_t moments (e.g., MY05a). In contrast, each of the SM simulations, including the diagnostic-N_0 simulations, shows a monopole pattern in N_{tr}, with the maximum located near the maximum in reflectivity near the core of the storm; the diagnostic relation for N_0 cannot fully represent all complex physical processes included in the DM scheme, including size sorting.

d. Squall-line case

Since the diagnostic relations were derived from a DM simulation of a supercell storm, the relative increase in similarity of the results of MY1DA and MY1DR to those of MY2 as compared with MY1A (shown in sections 5a–c) is perhaps not that surprising. A question one would ask is if these relationships are applicable to other types of convective systems, such as the squall line. To answer this question, we apply the diagnostic relations obtained above to a simulated squall line.

The squall line is again simulated using the ARPS model, in two dimensions. The domain is 700 km in the x direction and 20 km in the vertical direction. The grid spacing is 1 km in the horizontal direction. In the vertical direction there are 64 levels, with the vertical grid spacing

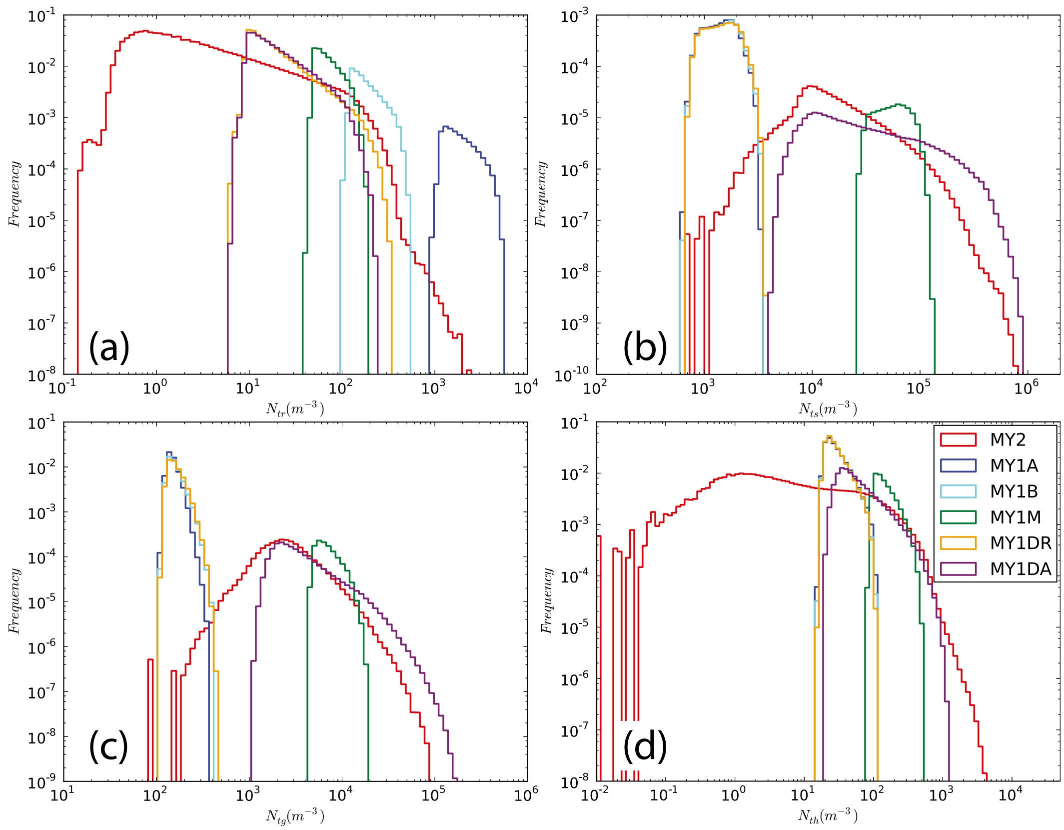

FIG. 12. Normalized histograms of (a) rain, (b) snow, (c) graupel, and (d) hail total number concentration N_t for MY2 (red), MY1A (blue), MY1B (cyan), MY1M (green), MY1DR (orange), and MY1DA (purple). Note the logarithmic scale for both axes. Histograms represent the accumulation of all grid points with $q > 1.0 \times 10^{-5}$ kg kg^{-1} from 3600 to 7200 s at 300-s intervals for each simulation.

being 100 m in the lowest 3 km and gradually increasing to 850 m at the model top. The simulations use the Weisman and Klemp (1982) analytic thermodynamic sounding. The wind profile used is -17.5 m s^{-1} at the surface, decreasing linearly to 0 m s^{-1} at a height of 5 km, giving 17.5 m s^{-1} of shear within the lowest 5 km. The wind speed remains zero above 5 km.

For the squall line, three separate simulations were run. The first simulation uses the original SM MY MP scheme and is denoted MY1A-Q (corresponding to MY1A). The second simulation uses the DM MY MP scheme (denoted MY2-Q, corresponding to MY2). The final simulation used the diagnostic-N_0 relations defined in section 3 for rain, snow, graupel, and hail. This simulation is denoted MY1DA-Q and corresponds to MY1DA. Each of these three simulations was run for 12 h.

The reflectivity fields shown in Fig. 13 represent the averages (relative to the leading edge of the surface gust front) over hours 3–6 of model time (note that this represents a mature squall line; in all cases the squall line becomes mature and quasi steady by 3 h into the simulation). The MY1A-Q simulation shows a strong cold pool and a rearward-tilted updraft, with the maximum updraft in the lower levels (Fig. 13a). MY2-Q shows a weaker, more elevated updraft, with a tilt close to neutral and a weaker cold pool (Fig. 13c). The mean reflectivity in MY1DA-Q shows a similar structure to that of MY2-Q, with a neutrally tilted updraft and the updraft maximum in the midlevels (as opposed to the lower levels in MY1A-Q; Fig. 13b). The height of the maximum reflectivity is within the lowest 3 km in both MY1DA-Q and MY2-Q, whereas the column of maximum reflectivity in MY1A-Q reaches a height of 7 km. The strong increase in reflectivity immediately below the melting layer in MY1DA-Q suggests a more vigorous cold-rain process, which is not seen in MY2-Q, suggesting that the diagnostic approach may not be optimally tuned for the squall-line case.

The cold pool in MY1DA-Q is weaker than in either MY1A-Q or MY2-Q. This can be seen in more detail in Fig. 14, which shows the time evolution of the surface cold pool in each of the simulations. It is clear that, while the cold pool is weakest in MY1DA-Q, the cold-pool evolution is closer to that of MY2-Q than to MY1A-Q, which

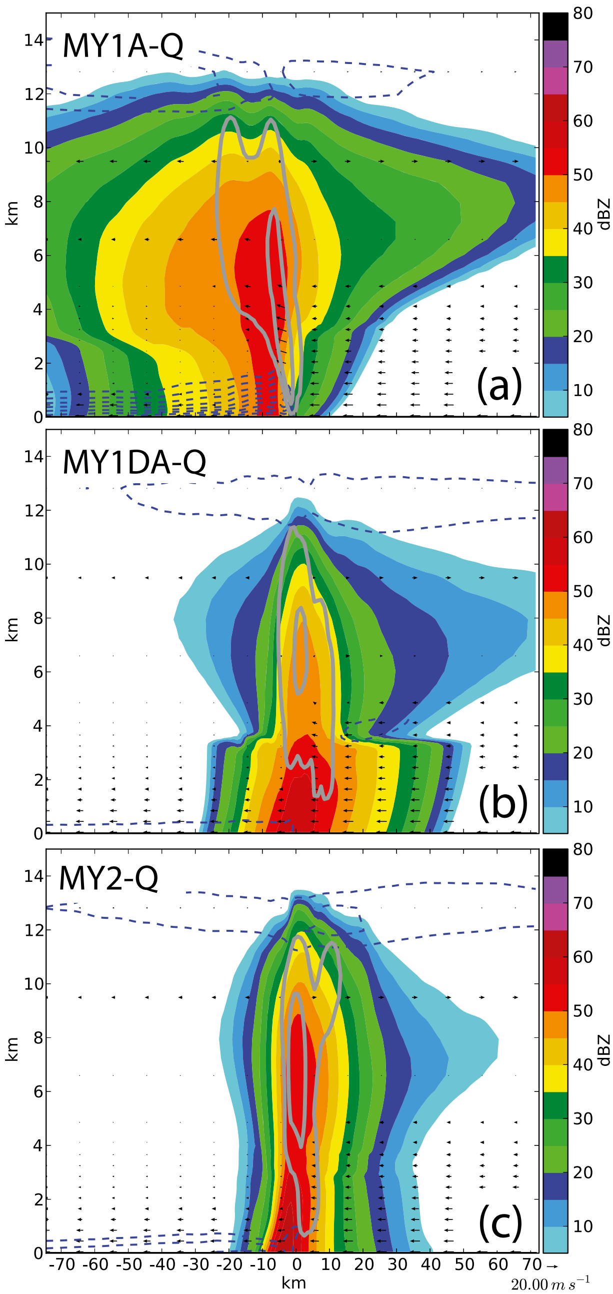

FIG. 13. Reflectivity (color filled), wind vectors (every 10 km in the horizontal direction; every fourth level in the vertical direction), vertical velocity (gray contours; only 1 and 5 m s^{-1} shown), and potential temperature perturbations (dashed blue contours; 1-K increment) averaged over hours 3–6 of the three squall-line simulations: (a) MY1A-Q, (b) MY1DA-Q, and (c) MY2-Q.

shows continued eastward growth after 2 h of simulation time, although MY1DA-Q and MY2-Q do not.

The results from MY1DA-Q more closely resemble those of MY2-Q than did those of MY1A-Q, but this fact does not necessarily mean that the MY1DA-Q results are more realistic. In fact, comparisons with the conceptual model for squall-line mesoscale convective systems presented in Houze (2004) suggest that the strong increase in reflectivity immediately below the melting level in Fig. 13 is not physically realistic. We do have the need to test further the diagnostic relations for N_0 with cases encompassing a range of precipitation types, though.

e. Sensitivity of MP processes to the diagnostic relations

To understand better the seemingly enhanced similarity of the simulations performed using the diagnostic relations to the DM simulations over the original SM simulations, we examine here how the diagnostic relations affect certain MP process rates for a range of mixing-ratio values from the supercell simulations. The N_0 values are set as follows: for the original SM scheme, constant values are used for all species (solid black lines in Figs. 1–4). For the diagnostic scheme, N_0 is diagnosed for each species using the relations derived in section 3. For the DM simulation, the N_0–W pairs from MY2 are sampled throughout the model domain over the entire range of times used to derive the diagnostic relations (see section 3).

Four MP processes are examined: rain evaporation, melting of snow, graupel, and hail. To examine these processes, the three sets of q–N_0 values defined above are used in the calculations of the equations of corresponding processes, taken from the MY schemes within the ARPS model. Each process is computed at a constant temperature of 5°C, an air density of 1 kg m^{-3}, and a water vapor mixing ratio of 5 g kg^{-1}. The results (Fig. 15) show that, for each of the processes examined, the diagnostic-N_0 approach better fits the envelope of points from the DM scheme than the original fixed-N_0 SM scheme does. For each of the processes, the fixed N_0 results in a line that does not overlap the set of points from the DM scheme (Figs. 15a–f). That the diagnostic-scheme line lies close to or within the spread of q–N_0 from the DM scheme serves to explain the similarity between the cold-pool structure from MY1DA and MY2 (and MY1DA-Q and MY2-Q).

Since the MP processes seem to be better represented (''better'' in terms of being ''closer to the MY2 reference'') in MY1DA, we suggest that the use of the diagnostic-N_0 method holds promise for simulations of other types of storms also.

6. Summary and conclusions

The overall goal of this study was to establish and utilize a relationship between the PSD parameters and the hydrometeor mass variables typically predicted in

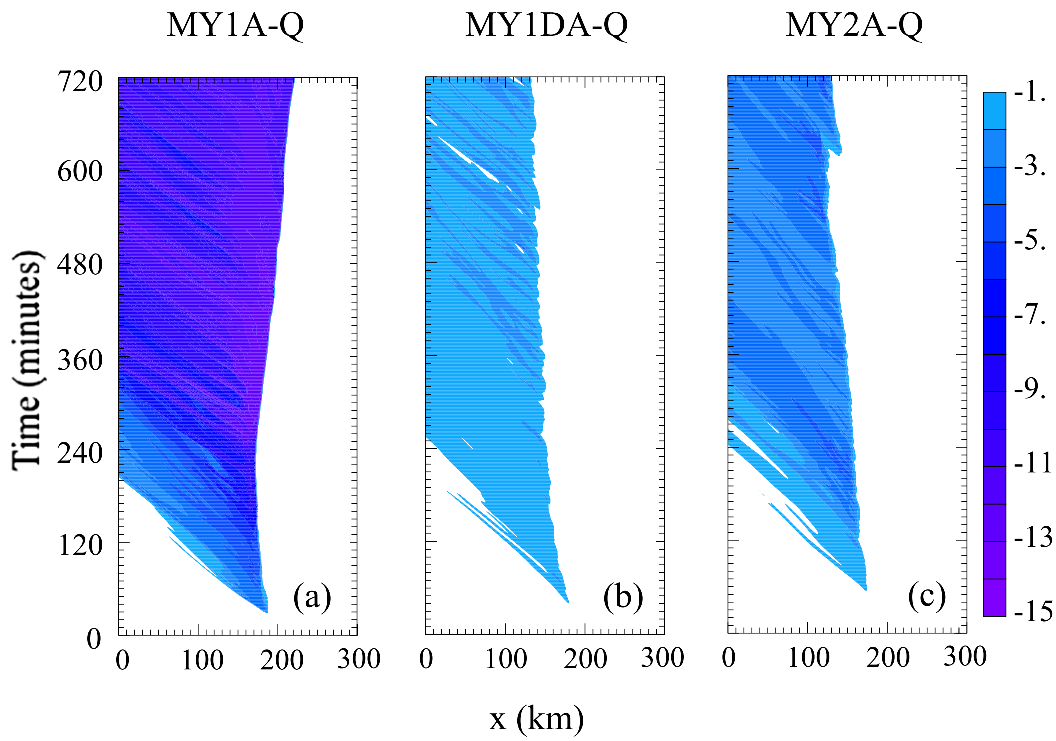

FIG. 14. Perturbation potential temperature θ' at the surface vs time (color filled), to show the evolution of the cold pool in the three squall-line simulations: (a) MY1A-Q, (b) MY1DA-Q, and (c) MY2-Q.

SM MP schemes in the hope of producing results that are closer to those of DM schemes. The PSD parameter chosen was the intercept parameter N_0. It has already been shown from disdrometer measurements that there is a measurable positive correlation between the two variables (Zhang et al. 2008), and in this study we derived such relationships on the basis of the output of an idealized two-moment simulation. The original SM Milbrandt and Yau MP scheme uses a fixed value for N_0 for each hydrometeor species. Two control simulations were run using the original single (MY1A) and DM (MY2) MP schemes, and these simulations were used as the basis against which all subsequent simulations in this study are compared.

Simply reducing the fixed value of N_{0r} by a factor of 20 (MY1B) showed improvements over MY1A in terms of producing results that are more closely aligned with those of the DM simulation (more realistic reflectivity structure, reduced cold-pool strength, reduced number concentration).

Diagnosing N_{0r} (MY1DR) produced simulations that are more consistent with MY2 than did the original fixed-N_{0r} SM simulation MY1A. These are limited to the lowest levels, however. The addition of a diagnostic relation for N_0 for the frozen hydrometeor categories (MY1DA) brings the simulation results further in line with MY2 than when N_{0r} only is diagnosed. Results with further increased consistency with MY2 are seen at low levels as well as above the melting layer because of increased consistency with MY2 in the structure of the frozen categories that can cause changes in the rain category through fallout and melting, among other processes.

The use of diagnostic relations for several frozen species was found to significantly increase the lateral extent of the storm in MY1DA over the other SM simulations. Extending the diagnostic-N_0 relation to the frozen hydrometeors also has a large positive impact on the cold-pool structure. It is known that altering N_0 of any of the hydrometeor distributions can have a large effect on the cold pool, because altering the shape of the distribution directly affects the rate of evaporative or melting cooling (e.g., Gilmore et al. 2004; van den Heever and Cotton 2004; Milbrandt and Yau 2006; Snook and Xue 2008; DXMY10).

While MY1DR produced a cold pool that was smaller in size and strength than that of MY1A, diagnosing the frozen category N_0 further reduced both the intensity and size of the cold pool, bringing the temperature deficit in line with that of MY2. The cold pool in MY2 was very weak, which agrees well with surface mesonet observations from the event (Markowski 2002); hence

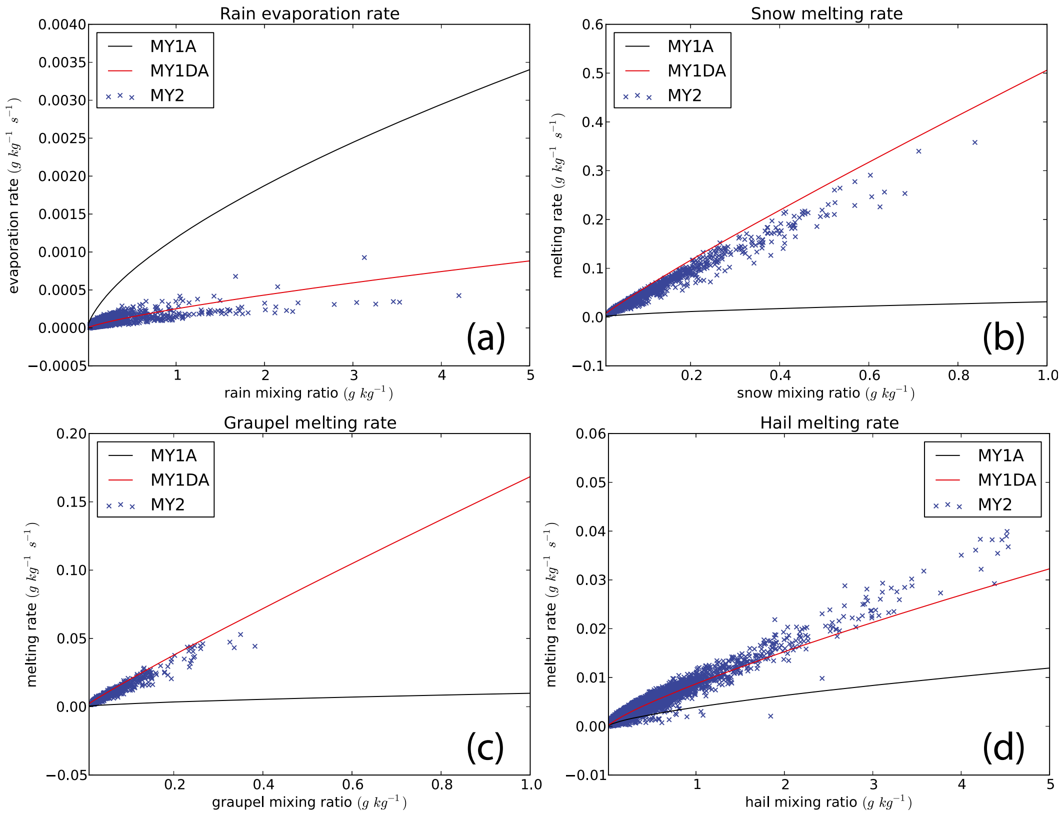

FIG. 15. The effect of the diagnostic intercept parameter on select MP processes: (a) rain evaporation, (b) snow melting, (c) graupel melting, and (d) hail melting. For each process, the results using three MP schemes are shown: MY1A (black line), MY1DA (red line), and MY2 (blue times signs).

the decreased cold-pool strength through diagnosing N_0 of the frozen species is encouraging.

Although the improved consistency of MY1DA with MY2 (as compared with MY1A) is encouraging, the diagnostic relations require testing to ensure that the derived relations are not too case specific. Similar results were obtained for the simulations of a 2D squall line. Using the diagnosed N_0 relations obtained from the reference supercell simulation, the reflectivity structure and cold-pool evolution of the SM simulation were brought closer to the results of the DM simulation for the squall line case also. An examination of four specific MP processes (evaporation of rain and melting of snow, graupel, and hail) using the diagnostic relations showed that their use brought the rates of all four processes closer to the rates that were evaluated using the DM scheme.

Although further testing is needed over a wider range of cases (e.g., severe convective storms, stratiform precipitation, and winter storms), the method examined in this paper shows considerable promise in bringing the results of a six-prognostic-variable SM MP scheme closer to a DM MP scheme, with a considerably lower computational cost relative to the DM scheme.

Acknowledgments. This study was primarily supported by NSF AGS-1046171 and by MOST 2013CB430103. The second author was partially supported by the National Research Council Postdoctoral Research Fellowship and by NSF Grant AGS-1137702. The third author was also supported by NSF Grants AGS-0802888, OCI-0905040, AGS-0941491, and AGS-0750790. Computations were carried out at the Oklahoma Supercomputing Center for Education and Research (OSCER) and at the Texas Advanced Computing Center (TACC). Some of the figures were generated using the free software package Matplotlib (Hunter 2007).

REFERENCES

Beard, K. V., D. B. Johnson, and D. Baumgardner, 1986: Aircraft observations of large raindrops in warm, shallow, convective clouds. *Geophys. Res. Lett.*, **13,** 991–994, doi:10.1029/GL013i010p00991.

Bolton, D., 1980: The computation of equivalent potential temperature. *Mon. Wea. Rev.*, **108,** 1046–1053, doi:10.1175/1520-0493(1980)108<1046:TCOEPT>2.0.CO;2.

Brock, F. V., K. C. Crawford, R. L. Elliott, G. W. Cuperus, S. J. Sandler, H. L. Johnson, and M. D. Eilts, 1995: The Oklahoma

Mesonet: A technical overview. *J. Atmos. Oceanic Technol.,* **12,** 5–19, doi:10.1175/1520-0426(1995)012<0005:TOMATO>2.0.CO;2.

Brooks, H. E., and C. A. Doswell, 2002: Deaths in the 3 May 1999 Oklahoma City tornado from a historical perspective. *Wea. Forecasting,* **17,** 354–361, doi:10.1175/1520-0434(2002)017<0354:DITMOC>2.0.CO;2.

Cao, Q., and G. Zhang, 2009: Errors in estimating raindrop size distribution parameters employing disdrometer and simulated raindrop spectra. *J. Appl. Meteor. Climatol.,* **48,** 406–425, doi:10.1175/2008JAMC2026.1.

——, ——, E. Brandes, T. Schuur, A. Ryzhkov, and K. Ikeda, 2008: Analysis of video disdrometer and polarimetric radar data to characterize rain microphysics in Oklahoma. *J. Appl. Meteor. Climatol.,* **47,** 2238–2255, doi:10.1175/2008JAMC1732.1.

Cohen, C., and E. W. McCaul Jr., 2006: The sensitivity of simulated convective storms to variations in prescribed single-moment microphysics parameters that describe particle distributions, sizes, and numbers. *Mon. Wea. Rev.,* **134,** 2547–2565, doi:10.1175/MWR3195.1.

Cooper, W. A., 1986: Ice initiation in natural clouds. *Precipitation Enhancement—A Scientific Challenge, Meteor. Monogr.,* No. 43, Amer. Meteor. Soc., 29–32. [Available online at http://journals.ametsoc.org/page/978-320-933876-65-1.]

Dawson, D. T., II, M. Xue, J. A. Milbrandt, M. K. Yau, and G. Zhang, 2007: Impact of multi-moment microphysics and model resolution on predicted cold pool and reflectivity intensity and structures in the Oklahoma tornadic supercell storms of 3 May 1999. *22nd Conf. on Weather Analysis and Forecasting/18th Conf. on Numerical Weather Prediction,* Salt Lake City, UT, Amer. Meteor. Soc., 10B.2. [Available online at https://ams.confex.com/ams/pdfpapers/124706.pdf.]

——, ——, ——, and ——, 2010: Comparison of evaporation and cold pool development between single-moment and multi-moment bulk microphysics schemes in idealized simulations of tornadic thunderstorms. *Mon. Wea. Rev.,* **138,** 1152–1171, doi:10.1175/2009MWR2956.1.

Doswell, C. A., III, and D. W. Burgess, 1993: Tornadoes and tornadic storms: A review of conceptual models. *The Tornado: Its Structure, Dynamics, Prediction, and Hazards, Geophys. Monogr.,* Vol. 79, Amer. Geophys. Union, 75–88.

Field, P. R., R. J. Hogan, P. R. A. Brown, A. J. Illingworth, T. W. Choularton, and R. J. Cotton, 2005: Parameterization of ice-particle size distributions for mid-latitude stratiform cloud. *Quart. J. Roy. Meteor. Soc.,* **131,** 1997–2017, doi:10.1256/qj.04.134.

Fujita, T. T., 1971: A proposed characterization of tornadoes and hurricanes by area and intensity. University of Chicago Dept. of Geophysical Sciences SMRP Research Paper 91, 42 pp.

Gilmore, M. S., J. M. Straka, and E. N. Rasmussen, 2004: Precipitation uncertainty due to variations in precipitation particle parameters within a simple microphysics scheme. *Mon. Wea. Rev.,* **132,** 2610–2627, doi:10.1175/MWR2810.1.

Heymsfield, A. J., A. Bansemer, S. L. Durden, R. L. Herman, and P. Bui, 2006: Ice microphysics observations in Hurricane Humberto: Comparison with non-hurricane-generated ice cloud layers. *J. Atmos. Sci.,* **63,** 288–308, doi:10.1175/JAS3603.1.

Houze, R. A., Jr., 2004: Mesoscale convective systems. *Rev. Geophys.,* **42,** RG4003, doi:10.1029/2004RG000150.

——, P. V. Hobbs, P. H. Herzegh, and D. B. Parsons, 1979: Size distributions of precipitation particles in frontal clouds. *J. Atmos. Sci.,* **36,** 156–162, doi:10.1175/1520-0469(1979)036<0156:SDOPPI>2.0.CO;2.

Hunter, J. D., 2007: Matplotlib: A 2D graphics environment. *Comput. Sci. Eng.,* **9,** 90–95, doi:10.1109/MCSE.2007.55.

Jung, Y., M. Xue, and G. Zhang, 2010: Simulations of polarimetric radar signatures of a supercell storm using a two-moment bulk microphysics scheme. *J. Appl. Meteor. Climatol.,* **49,** 146–163, doi:10.1175/2009JAMC2178.1.

Kumjian, M. R., and A. V. Ryzhkov, 2008: Polarimetric signatures in supercell thunderstorms. *J. Appl. Meteor. Climatol.,* **47,** 1940–1961, doi:10.1175/2007JAMC1874.1.

——, and ——, 2009: Storm-relative helicity revealed from polarimetric radar measurements. *J. Atmos. Sci.,* **66,** 667–685, doi:10.1175/2008JAS2815.1.

——, and ——, 2012: The impact of size sorting on the polarimetric radar variables. *J. Atmos. Sci.,* **69,** 2042–2060, doi:10.1175/JAS-D-11-0125.1.

Mallet, C., and L. Barthes, 2009: Estimation of gamma raindrop size distribution parameters: Statistical fluctuations and estimation errors. *J. Atmos. Oceanic Technol.,* **26,** 1572–1584, doi:10.1175/2009JTECHA1199.1.

Markowski, P. M., 2002: Mobile mesonet observations on 3 May 1999. *Wea. Forecasting,* **17,** 430–444, doi:10.1175/1520-0434(2002)017<0430:MMOOM>2.0.CO;2.

Marshall, J. S., and W. M. Palmer, 1948: The distribution of raindrops with size. *J. Meteor.,* **5,** 165–166, doi:10.1175/1520-0469(1948)005<0165:TDORWS>2.0.CO;2.

Milbrandt, J. A., and M. K. Yau, 2005a: A multimoment bulk microphysics parameterization. Part I: Analysis of the role of the spectral shape parameter. *J. Atmos. Sci.,* **62,** 3051–3064, doi:10.1175/JAS3534.1.

——, and ——, 2005b: A multimoment bulk microphysics parameterization. Part II: A proposed three-moment closure and scheme description. *J. Atmos. Sci.,* **62,** 3065–3081, doi:10.1175/JAS3535.1.

——, and ——, 2006: A multimoment bulk microphysics parameterization. Part IV: Sensitivity experiments. *J. Atmos. Sci.,* **63,** 3137–3159, doi:10.1175/JAS3817.1.

Morrison, H., and J. A. Milbrandt, 2011: Comparison of two-moment bulk microphysics schemes in idealized supercell thunderstorm simulations. *Mon. Wea. Rev.,* **139,** 1103–1130, doi:10.1175/2010MWR3433.1.

——, J. A. Curry, and V. I. Khvorostyanov, 2005: A new double-moment microphysics parameterization for application in cloud and climate models. Part I: Description. *J. Atmos. Sci.,* **62,** 1665–1677, doi:10.1175/JAS3446.1.

——, G. Thompson, and V. Tatarskii, 2009: Impact of cloud microphysics on the development of trailing stratiform precipitation in a simulated squall line: Comparison of one- and two-moment schemes. *Mon. Wea. Rev.,* **137,** 991–1007, doi:10.1175/2008MWR2556.1.

Posselt, D. J., and T. Vukicevic, 2010: Robust characterization of model physics uncertainty for simulations of deep moist convection. *Mon. Wea. Rev.,* **138,** 1513–1535, doi:10.1175/2009MWR3094.1.

——, and C. H. Bishop, 2012: Nonlinear parameter estimation: Comparison of an ensemble Kalman smoother with a Markov chain Monte Carlo algorithm. *Mon. Wea. Rev.,* **140,** 1957–1974, doi:10.1175/MWR-D-11-00242.1.

Roebber, P. J., D. M. Schultz, and R. Romero, 2002: Synoptic regulation of the 3 May 1999 tornado outbreak. *Wea. Forecasting,* **17,** 399–429, doi:10.1175/1520-0434(2002)017<0399:SROTMT>2.0.CO;2.

Snook, N., and M. Xue, 2008: Effects of microphysical drop size distribution on tornadogenesis in supercell thunderstorms. *Geophys. Res. Lett.,* **35,** L24803, doi:10.1029/2008GL035866.

Snyder, J. C., H. B. Bluestein, Y. Jung, S. J. Frasier, and V. Venkatesh, 2010: The structure and time evolution of polarimetric signatures in severe convective storms based on high-resolution numerical simulations and data from a mobile, dual-polarized, X-band Doppler radar. *25th Conf. on Severe Local Storms,* Denver, CO, Amer. Meteor. Soc., P8.8. [Available online at https://ams.confex.com/ams/pdfpapers/176247.pdf.]

Speheger, D. A., C. A. Doswell, and G. J. Stumpf, 2002: The tornadoes of 3 May 1999: Event verification in central Oklahoma and related issues. *Wea. Forecasting,* **17,** 362–381, doi:10.1175/1520-0434(2002)017<0362:TTOMEV>2.0.CO;2.

Straka, J. M., and E. R. Mansell, 2005: A bulk microphysics parameterization with multiple ice precipitation categories. *J. Appl. Meteor.,* **44,** 445–466, doi:10.1175/JAM2211.1.

Thompson, R. L., and R. Edwards, 2000: An overview of environmental conditions and forecast implications of the 3 May 1999 tornado outbreak. *Wea. Forecasting,* **15,** 682–699, doi:10.1175/1520-0434(2000)015<0682:AOOECA>2.0.CO;2.

Tokay, A., and D. A. Short, 1996: Evidence from tropical raindrop spectra of the origin of rain from stratiform versus convective clouds. *J. Appl. Meteor.,* **35,** 355–371, doi:10.1175/1520-0450(1996)035<0355:EFTRSO>2.0.CO;2.

Tong, M., and M. Xue, 2008a: Simultaneous estimation of microphysical parameters and atmospheric state with simulated radar data and ensemble square root Kalman filter. Part I: Sensitivity analysis and parameter identifiability. *Mon. Wea. Rev.,* **136,** 1630–1648, doi:10.1175/2007MWR2070.1.

——, and ——, 2008b: Simultaneous estimation of microphysical parameters and atmospheric state with simulated radar data and ensemble square root Kalman filter. Part II: Parameter estimation experiments. *Mon. Wea. Rev.,* **136,** 1649–1688, doi:10.1175/2007MWR2071.1.

Ulbrich, C. W., 1983: Natural variations in the analytical form of the raindrop size distributions. *J. Appl. Meteor.,* **22,** 1764–1775, doi:10.1175/1520-0450(1983)022<1764:NVITAF>2.0.CO;2.

van den Heever, S. C., and W. R. Cotton, 2004: The impact of hail size on simulated supercell storms. *J. Atmos. Sci.,* **61,** 1596–1609, doi:10.1175/1520-0469(2004)061<1596:TIOHSO>2.0.CO;2.

van Lier-Walqui, M., T. Vukicevic, and D. J. Posselt, 2012: Quantification of cloud microphysical parameterization uncertainty using radar reflectivity. *Mon. Wea. Rev.,* **140,** 3442–3466, doi:10.1175/MWR-D-11-00216.1.

——, ——, and ——, 2014: Linearization of microphysical parameterization uncertainty using multiplicative process perturbation parameters. *Mon. Wea. Rev.,* **142,** 401–413, doi:10.1175/MWR-D-13-00076.1.

Van Weverberg, K., 2013: Impact of environmental instability on convective precipitation uncertainty associated with the nature of the rimed ice species in a bulk microphysics scheme. *Mon. Wea. Rev.,* **141,** 2841–2849, doi:10.1175/MWR-D-13-00036.1.

——, N. P. M. van Lipzig, and L. Delobbe, 2011: The impact of size distribution assumptions in a bulk one-moment microphysics scheme on simulated surface precipitation and storm dynamics during a low-topped supercell case in Belgium. *Mon. Wea. Rev.,* **139,** 1131–1147, doi:10.1175/2010MWR3481.1.

——, A. M. Vogelmann, H. Morrison, and J. A. Milbrandt, 2012: Sensitivity of idealized squall-line simulations to the level of complexity used in two-moment bulk microphysics schemes. *Mon. Wea. Rev.,* **140,** 1883–1907, doi:10.1175/MWR-D-11-00120.1.

Waldvogel, A., 1974: The N_0 jump of raindrop spectra. *J. Atmos. Sci.,* **31,** 1067–1078, doi:10.1175/1520-0469(1974)031<1067:TJORS>2.0.CO;2.

Weisman, M. L., and J. B. Klemp, 1982: The dependence of numerically simulated convective storms on vertical wind shear and buoyancy. *Mon. Wea. Rev.,* **110,** 504–520, doi:10.1175/1520-0493(1982)110<0504:TDONSC>2.0.CO;2.

Xue, M., 2000: High-order monotonic numerical diffusion and smoothing. *Mon. Wea. Rev.,* **128,** 2853–2864, doi:10.1175/1520-0493(2000)128<2853:HOMNDA>2.0.CO;2.

——, K. K. Droegemeier, and V. Wong, 2000: The Advanced Regional Prediction System (ARPS)—A multiscale nonhydrostatic atmospheric simulation and prediction tool. Part I: Model dynamics and verification. *Meteor. Atmos. Phys.,* **75,** 161–193, doi:10.1007/s007030070003.

——, ——, ——, A. Shapiro, K. Brewster, F. Carr, D. Weber, Y. Liu, and D. Wang, 2001: The Advanced Regional Prediction System (ARPS)—A multiscale nonhydrostatic atmospheric simulation and prediction tool. Part II: Model physics and applications. *Meteor. Atmos. Phys.,* **76,** 143–165, doi:10.1007/s007030170027.

Yussouf, N., E. R. Mansell, L. J. Wicker, D. M. Wheatley, and D. J. Stensrud, 2013: The ensemble Kalman filter analyses and forecasts of the 8 May 2003 Oklahoma City tornadic supercell storm using single- and double-moment microphysics schemes. *Mon. Wea. Rev.,* **141,** 3388–3412, doi:10.1175/MWR-D-12-00237.1.

Yuter, S. E., and R. A. Houze, 1997: Measurements of raindrop size distributions over the Pacific warm pool and implications for *Z*–*R* relations. *J. Appl. Meteor.,* **36,** 847–867, doi:10.1175/1520-0450(1997)036<0847:MORSDO>2.0.CO;2.

Zhang, G., J. Vivekanandan, and E. Brandes, 2001: A method for estimating rain rate and drop size distribution from polarimetric radar measurements. *IEEE Trans. Geosci. Remote Sens.,* **39,** 830–841, doi:10.1109/36.917906.

——, ——, E. A. Brandes, R. Meneghini, and T. Kozu, 2003: The shape–slope relation in observed gamma raindrop size distributions: Statistical error or useful information? *J. Atmos. Oceanic Technol.,* **20,** 1106–1119, doi:10.1175/1520-0426(2003)020<1106:TSRIOG>2.0.CO;2.

——, M. Xue, Q. Cao, and D. Dawson, 2008: Diagnosing the intercept parameter for exponential raindrop size distribution based on video disdrometer observations: Model development. *J. Appl. Meteor. Climatol.,* **47,** 2983–2992, doi:10.1175/2008JAMC1876.1.